



Contents lists available at ScienceDirect

## Advanced Powder Technology

journal homepage: [www.elsevier.com/locate/apt](http://www.elsevier.com/locate/apt)

Original Research Paper

# Preparation of nitrogen-doped aluminium titanate ( $\text{Al}_2\text{TiO}_5$ ) nanostructures: Application to removal of organic pollutants from aqueous media

Abolfazl Azarniya<sup>a,\*</sup>, Mahdi Zekavat<sup>a</sup>, Mohammad Soltaninejad<sup>a</sup>, Fatemeh Bakhshandeh<sup>a</sup>,  
Hamid Reza Madaah Hosseini<sup>a,\*</sup>, Shima Kashani<sup>a</sup>, Chinnappan Amutha<sup>b</sup>,  
Seyed Khatiboleslam Sadrnezhad<sup>a</sup>, Seeram Ramakrishna<sup>b</sup>

<sup>a</sup> Department of Materials Science and Engineering, Sharif University of Technology, P.O. Box 11155-9466, Azadi Avenue, Tehran, Iran

<sup>b</sup> Department of Mechanical Engineering, National University of Singapore, 9 Engineering Drive 1, Singapore 117576, Singapore

## ARTICLE INFO

## Article history:

Received 30 January 2020

Received in revised form 29 May 2020

Accepted 11 June 2020

Available online xxxxx

## Keywords:

Nitrogen doping

Aluminium titanate ( $\text{Al}_2\text{TiO}_5$ )

Photocatalysis

Semiconductor

Band gap narrowing

## ABSTRACT

Recently, aluminum titanate ( $\text{Al}_2\text{TiO}_5$ )-based nanostructures have been proved to serve as an efficient photocatalytic material with satisfactory photodegradation capacity. In this study, the citrate sol-gel method was used to synthesize these nanostructures and inspect the significant impacts of nitrogen-doping-originated crystalline defects on their photocatalytic performance in some details for the first time. The results indicated that the penetration of nitrogen atoms into AT crystal lattice, depending on the nitriding time and temperature, can induce a great deal of the residual stress and result in propagating the existing cracks and breaking down the particles. The XPS and FTIR results confirmed the formation of some new bonds in the crystal structure (including O-Ti-N and Ti-N), the substitutional and interstitial replacement of nitrogen atoms with oxygen atoms, oxygen vacancies, and the attachment of nitrogen species at superficial oxygen sites. These events may vary the bandgap values from 2.88 eV for pristine AT to 2.73 eV for the nitrided one, thereby manipulating the charge carrier recombination rate and activation of superficial catalytic reactions in the particles. Numerically, the band structure variations can efficiently increase the photodegradation efficiency of methylene blue (MB) and apparent rate constant (k) by 1.4 times (from 38.9 to 55.9%) and 1.8 times (from 0.0038 to 0.0068  $\text{min}^{-1}$ ), respectively. Finally, the results show that the synthesized photocatalyst can successfully compete with  $\text{TiO}_2$ -based photocatalysts in terms of photocatalytic performance.

© 2020 The Society of Powder Technology Japan. Published by Elsevier B.V. and The Society of Powder Technology Japan. All rights reserved.

## 1. Introduction

Recently, many research works have concentrated on the removal of organic pollutants from the natural environment, especially water resources. The photocatalysis based on the semiconductor technology is deemed as a promising strategy to address this challenge. A variety of semiconductors have been successfully designed and broadly exploited for this purpose. Among them, metal oxides such as  $\text{TiO}_2$  [1,2],  $\text{ZnO}$  [3,4], and  $\text{WO}_3$  [5,6] have attracted more attention than their counterparts due to high thermal and chemical stability, favorable degradation capacity and environment-friendly features [7,8].

When a semiconductor photocatalyst is exposed to the incident radiation, the electron in the valence band can be excited to the conduction band by capturing a photon whose energy is the equivalence of or higher than that of the band gap, leaving behind holes in the valence band. Subsequently, these generated electron-hole pairs take part in some specified redox reactions and release some active species such as hydroxyl radicals ( $\cdot\text{OH}$ ),  $\text{H}^+$ , and superoxide radicals ( $\cdot\text{O}_2$ ). These species are responsible for the decomposition of organic pollutants into non-toxic products [9–12].

Along with extensive studies on the conventional photocatalytic materials, a new generation of semiconductors has been recently developed for the photocatalytic applications [13]. While estimating the optical band gap of  $\text{Al}_2\text{TiO}_5$  (AT) as approximately 2.89 eV, Bakhshandeh et al. [14] proposed the AT-rich ceramic nanocomposite as an appropriate photocatalyst as efficient as anatase or superior. It was the first time that the AT nanostructure was

\* Corresponding authors.

E-mail addresses: [Abolfazl.azarniya@student.sharif.edu](mailto:Abolfazl.azarniya@student.sharif.edu), [Abolfazl.azarniya@nus.edu](mailto:Abolfazl.azarniya@nus.edu) (A. Azarniya), [madaah@sharif.edu](mailto:madaah@sharif.edu) (H. Reza Madaah Hosseini).

<https://doi.org/10.1016/j.apt.2020.06.020>

0921-8831/© 2020 The Society of Powder Technology Japan. Published by Elsevier B.V. and The Society of Powder Technology Japan. All rights reserved.

exposed to the UV irradiation and its photoactivity was explored in the presence of organic dyes. Accordingly, the maximum photodegradation rate of the dye can be achieved whenever the AT relative content reaches a summit. The novelty of this case study necessitates more profound studies, aimed at improving the photocatalytic activity of the AT-based nanocomposite.

The defect engineering and doping with metals (such as Fe, Ni, and Co) and non-metallic elements (such as C, F, N, S, or I) are broadly suggested approaches to enhance the photocatalytic response of the semiconductors [15–17]. The metal doping in some metallic oxides such as TiO<sub>2</sub> has not been further developed, because the existence of metallic atoms in the crystalline lattice increases the recombination rate of photo-induced electron-hole pairs [18]. In contrast, doping with non-metals is much favored due to their effectiveness in narrowing the band gap of TiO<sub>2</sub> [19,20]. However, the toxicity of F anions, elevated temperatures needed for C-doping, and the natural poisoning of the TiO<sub>2</sub> catalyst as a result of the S doping have limited their applications. Among the non-metal elements, N-doping is the most favorable route [21,22]. Using the computational method, Asahi et al. [23,24] proved that N-doping of TiO<sub>2</sub> through the substitutional oxygen sites generates additional N 2p energy states, a little above the valence band maximum, which finally narrows the forbidden zone. The nitrogen incorporation into the TiO<sub>2</sub> lattice also decreases the formation energy of oxygen vacancies, thereby increasing the chance of oxygen vacancies formation [25]. By manipulating the relative concentration of the oxygen vacancies in the superficial and bulk regions, the separation efficiency of photo-induced electron-hole pairs can improve and result in enhanced photoactivity [26–28].

Up to now, a variety of techniques have been designed and developed to introduce nitrogen atoms into crystalline lattices [17,29]. For example, the annealing in a nitrogen-rich atmosphere is a cost-effective option. Some of the literature have introduced the annealing in a gaseous NH<sub>3</sub>-containing atmosphere as a successful technique to modify the electronic and photocatalytic characteristics of metal oxides such as TiO<sub>2</sub> and ZrO<sub>2</sub> [30–32]. As a typical case study, Fàbrega et al. [33] drew a comparison between the annealing of TiO<sub>2</sub> in the H<sub>2</sub>-N<sub>2</sub> atmosphere and that of this material at the NH<sub>3</sub>-rich one. It was concluded that using an H<sub>2</sub>-N<sub>2</sub> atmosphere increases the total density of interfacial oxygen vacancies and keeps the N-doping level at a low amount, leading to higher photocatalytic activity of TiO<sub>2</sub>, but the annealing in a gaseous ammonia atmosphere gives rise to the formation of unfavorable TiN phase and diminishes the photocatalytic efficiency. Similarly, there are other research works reporting the formation of the TiN phase in the presence of NH<sub>3</sub> [32,34]. Sarkar et al. [35] investigated the effect of various annealing atmospheres (i.e. N<sub>2</sub>, H<sub>2</sub>, and NH<sub>3</sub>) on the photocatalytic activity of TiO<sub>2</sub> and indicated that the results associated to a given test condition could not be generalized to another one with different variables. The strong dependency of photocatalytic performance on the type of precursor used for N-doped material is a compelling reason for this fact [36].

To the best of our knowledge, no research work has concentrated on the nitrogen doping of AT-based nanostructures and its effect on the phase composition and photocatalytic performance. In the present work, an AT-based nanocomposite was synthesized and annealed under the N<sub>2</sub> flow for the first time to cast light on the potential impact of nitriding on its photocatalytic behavior. The microstructure and characterization studies of N-doped ceramics were performed to improve the photocatalytic degradation of methylene blue (MB) under the UV irradiation and evaluate any variations in their photocatalytic response. The results indicated that the simultaneous presence of oxygen vacancies and nitrogen species in the crystalline structure of AT-based

nanostructures provides complex conditions for systematically correlating the photocatalytic performance with annealing parameters.

## 2. Experimental procedure

### 2.1. Synthesis of AT-based nanostructures

The citrate sol–gel method under a continuous flow of argon gas was used to synthesize AT-based nanostructures. The used chemical sources included anhydrous aluminum chloride (AlCl<sub>3</sub>), titanium tetraisopropoxide (TTIP or C<sub>16</sub>H<sub>36</sub>O<sub>4</sub>Ti), absolute ethanol (C<sub>2</sub>H<sub>5</sub>OH) and anhydrous citric acid (C<sub>6</sub>H<sub>8</sub>O<sub>7</sub>). The Merck company provided all raw materials. Full details of the synthesis process have been presented in [14,37–39].

### 2.2. Nitriding of the synthesized powder

To penetrate nitrogen atoms into AT nanostructures, the samples were exposed to a continuous flow of nitrogen gas through a U-shaped tube inside a furnace. The procedure was a crucible heating method with highly pure N<sub>2</sub> gas (purity: 99.9%). In all experiments, the heating rate and gas flow rate were 10 sccm and 10 °C/min, respectively. Nine samples were prepared by nitriding at 300, 400, and 500 °C for 30, 60, and 180 min. Table 1 gives a concise list of the processing conditions for the test samples and their related abbreviations.

### 2.3. Phase characterization

The morphology and phase structure of the as-synthesized AT powder were examined by X-ray diffraction (XRD, Philips Model PW3710, Netherland) analysis, field-emission scanning electron microscopy (FE-SEM, Philips Model XL30, Netherlands) equipped with energy-dispersive spectroscopy (EDS), and high-resolution transmission electron microscopy (HR-TEM, Jeol Jem-2100). Similar characterization was carried out for nitrided samples to determine what variations in morphology, phase analysis, and penetrated nitrogen content occur during the nitriding treatment. The nitrogen content of each sample was measured three times by EDS from three different points, and average values were reported in this work. The average grain size distribution of all powdery samples was determined by using the ImageJ software based on the FESEM micrographs, and was plotted versus the nitriding temperature and time. Also, x-ray photoelectron spectroscopy (XPS, Thermo ESCALAB 250, USA) was employed to determine which bonds are formed in the nitrided nanostructures.

**Table 1**

A summary of practical conditions for test samples and pertinent abbreviations.

Abbreviations	Processing conditions	Nitriding time	Nitriding temperature
U900	Non-nitrides (as-synthesized)	–	–
N300-30	Nitrided	30 min	300 °C
N300-60	Nitrided	60 min	300 °C
N300-180	Nitrided	180 min	300 °C
N400-30	Nitrided	30 min	400 °C
N400-60	Nitrided	60 min	400 °C
N400-180	Nitrided	180 min	400 °C
N500-30	Nitrided	30 min	500 °C
N500-60	Nitrided	60 min	500 °C
N500-180	Nitrided	180 min	500 °C

## 2.4. Optical characterization

To evaluate the photocatalytic activity of the samples, the photodegradation test was measured by methylene blue (MB) under the UV irradiation. All the experiments were carried out in a handmade reactor consisting of two 8 W Hitachi UVA lamps, with a maximum peak at 369 nm. At room temperature, 0.05 g of the as-synthesized sample was added to 100 ml of 10<sup>-5</sup> M MB aqueous solution. The distance of the prepared suspension surface from the light source was fixed at 13 cm before the irradiation. The suspension was placed in darkness and stirred for 1 h to achieve the adsorption/desorption equilibrium between the MB and photocatalyst. Aliquots of the samples were taken at certain time intervals (i.e. 20, 40, 60, 90, and 120 min) and subsequently centrifuged and filtered to remove the remaining catalyst particles. Then, the concentration of the remaining MB was measured by a UV-vis spectrophotometer (6705 JENWAY).

To study the optical characteristics of the samples and calculate their band gap energy values, UV-vis diffuse reflectance (DRS) of the samples was measured by an avantes spectrophotometer (DRS, Avaspec-2048-TEC) using BaSO<sub>4</sub> as a reference. To further investigate the fate of photo-generated electron-hole pairs during the photocatalysis, the photoluminescence (PL) spectrum of the samples was also measured by an avantes spectrophotometer (Avaspec-2048-TEC) under the excitation light of 355 nm. Fig. 1 shows the practical steps of the present research.

## 2.5. Photoelectrochemical characterization

To scientifically elucidate why the nitriding can tailor the photocatalytic performance of hybrid AT nanostructures, the photoelectrochemical tests were conducted. In the Mott-Schottky (MS) test, the flat band potential values and doping density of the samples were determined by plotting  $C^{-2}$  against the applied voltage  $V$ , where  $C$  is the observed capacitance. In this study, the powdery samples were examined on fluorine-doped tin oxide at the frequency of 100 Hz. Also, Electrochemical Impedance Spectroscopy (EIS) investigations were carried out at room temperature using a conventional two-electrode system (i.e. Pt as a working electrode

and Ag/AgCl as the counter electrode) by applying an AC voltage in the frequency range of 1 Hz– 100 KHz. The photocurrent response of the samples was also measured to plot the variation of photo-induced current against the applied potential difference.

## 3. Results and discussion

### 3.1. Phase characterization

#### 3.1.1. Characterization of as-prepared samples

In general, the formation mechanism and synthesis conditions can significantly influence the morphology and geometrical specifications of nanostructures. Fig. 2 shows SEM and TEM images of the as-synthesized AT-based nanostructure, as well as a nanoscale elemental map of constituent atoms, i.e. Al, Ti, and O. As seen, the particles bear the blocky-shaped morphology with worm-like microstructure whose units correspond to some nanometric thermodynamically stable phases. As seen from the obtained elemental map, these phases are uniformly dispersed into the as-prepared nanostructure, forming micro-sized coarse particles. The XRD analysis confirms the presence of AT as the dominant phase as well as Al<sub>2</sub>O<sub>3</sub> and TiO<sub>2</sub> as impurities (Fig. 3) whose average size is relatively 50 nm, with a weak bond to neighboring units. The fragmentation of the coarse AT particles into nanometric ones during the ultrasonication in an aqueous medium is the compelling evidence of weak bonding between the constituent units.

#### 3.1.2. Characterization of nitrided samples

**3.1.2.1. SEM and XRD analyses.** To evaluate whether the nitrogen penetration can affect the morphology, chemical stability, and mean particle size of the powdery samples, all the specimens were examined by EDS analysis and SEM. Fig. 4a shows the variation trend of nitrogen content as a function of nitriding time and temperature. These data have been obtained by the EDS analysis and averaged out over five different measurements for each powdery sample. As seen, the extension of nitriding time at a constant temperature first increases and then decreases the penetration of nitrogen atoms into the AT-based nanostructure. Although it seems that this trend has a kinetic origin and needs further

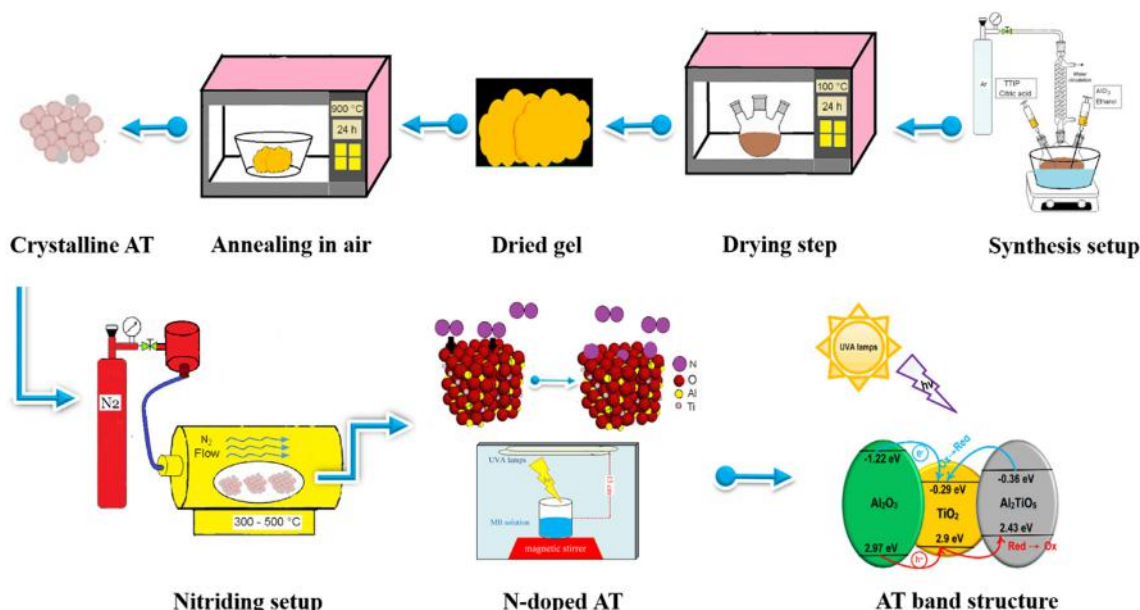


Fig. 1. A schematic illustration of the synthesis, nitriding, and photocatalytic test of AT-based heterostructures.

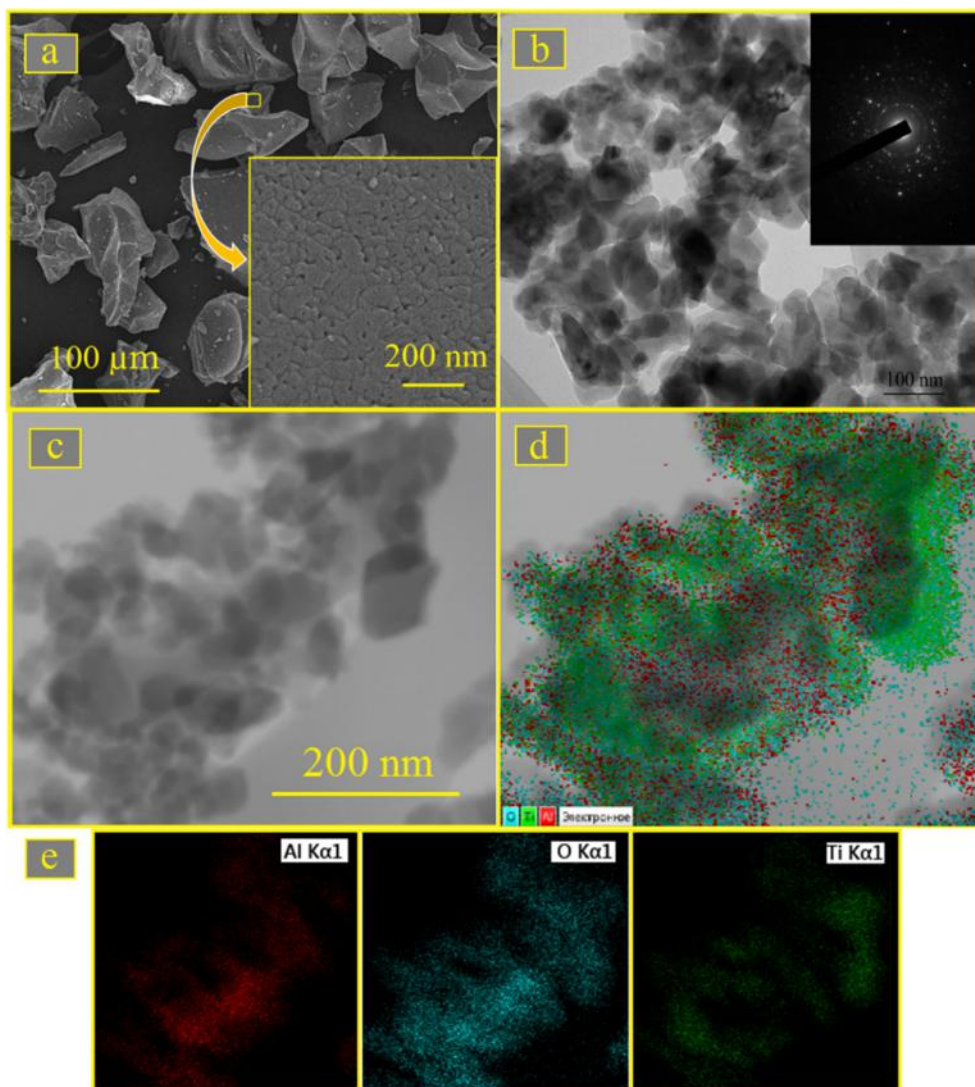


Fig. 2. (a) FESEM image and (b,c) TEM images of as-synthesized AT ceramic, and (d,e) elemental map of Ti, O, and Al in the U900 sample.

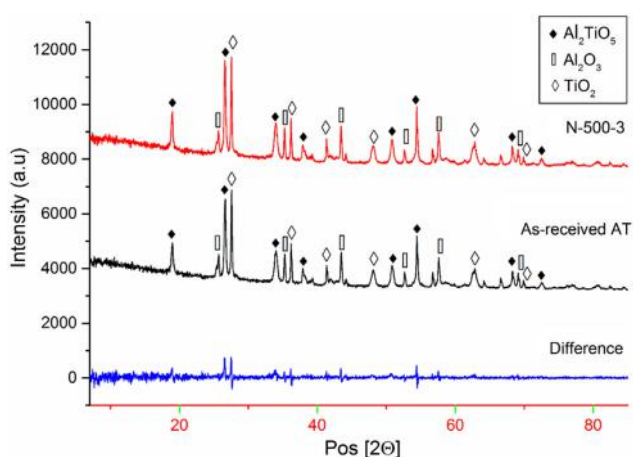
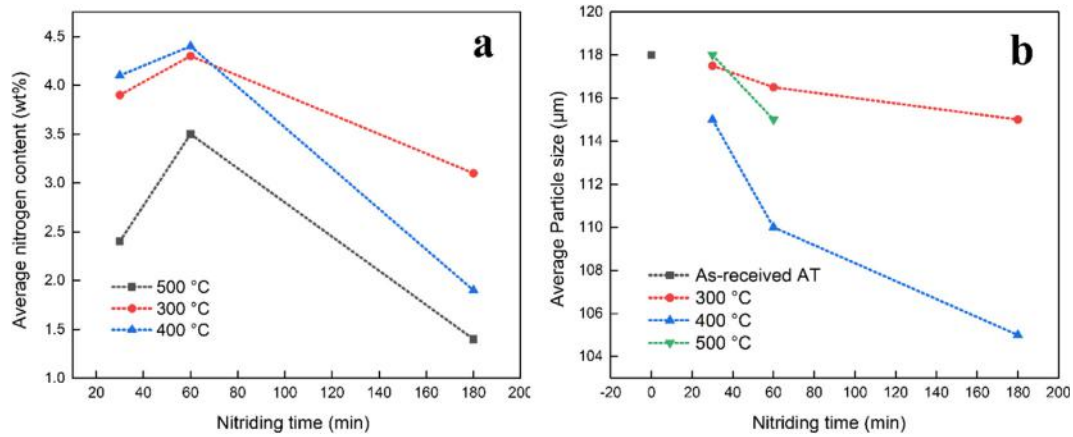


Fig. 3. XRD patterns of samples U900 and N500-180, indicating the presence of AT,  $\text{TiO}_2$ , and  $\text{Al}_2\text{O}_3$  phases; The intensity difference between these two patterns have been depicted, showing which peaks have been heightened after nitriding.

overall variation of the AT particle size with nitriding conditions for all annealed samples. As seen, the extension of nitriding time at a constant temperature results in the particles fracturing into smaller ones. This fact is shown in Fig. 5(a-b). Seemingly, the propagation of ubiquitous microcracks during the annealing and subsequent particle fracturing can arise from two main origins: (i) AT is thermally anisotropic and can yield detrimental cracks during the cooling step from the annealing temperature; and (ii) The diffusion of nitrogen atoms into AT crystal lattice can induce a great deal of residual stress and result in propagating the existing cracks if the stress level exceeds the energy required for the formation of new surfaces in AT particles. This fact has been confirmed by XRD results. Fig. 3 shows the XRD analysis of the sample N500-180, where there is no significant difference between the XRD result of the as-received AT and that of the nitrided sample N500-180. It indicates that the nitriding is not able to considerably change the phase content and type. The XRD curves can be used to evaluate the residual strain induced during the nitriding of the AT crystal structure. AT bears an orthorhombic unit cell so that its lattice parameters abide by the following equation:

$$\frac{1}{d_{hkl}^2} = \frac{h^2}{a^2} + \frac{k^2}{b^2} + \frac{l^2}{c^2} \quad (1)$$

investigations in future research works, the particles fragmentation during the nitriding can play a role in it. Fig. 4b shows the



**Fig. 4.** (a) The variation of doped nitrogen content as a function of nitriding time and temperature, (b) The variation of AT-based particle size as a function of nitriding time and temperature. The nitriding process fractures the particles into smaller ones.

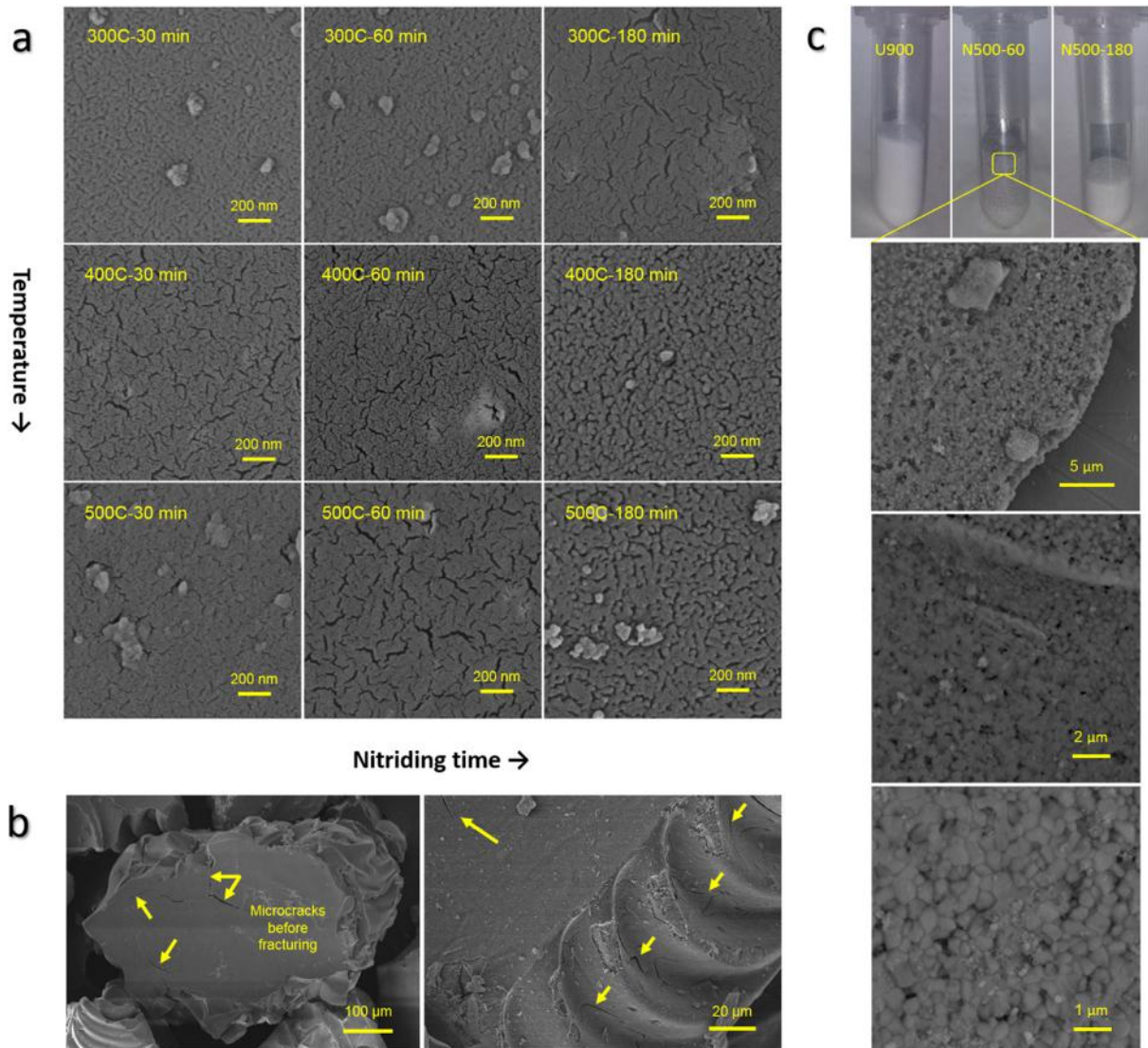


**Fig. 5.** (a) The propagating ubiquitous sub-micron cracks throughout the nitrided AT-based particles after different nitriding treatments, (b) The fractured particles after the propagation of micro-sized cracks, and (c) Macroscopic images of the samples U900, N500-60, and N500-180, showing black particles with high doped-nitrogen content, as well as FE-SEM images of black particles distributed inside the high doped-nitrogen powders e.g. N500-60.

where  $a$ ,  $b$ , and  $c$  are the lattice constants,  $h$ ,  $k$ , and  $l$  are the miller indices, and  $d_{hkl}$  is the distance between  $(hkl)$  planes. For a certain plane  $(hkl)$ ,  $d_{hkl}$  can be calculated from the XRD pattern by Eq. (2):

$$d_{hkl} = \frac{n\lambda}{2 \sin \theta_{hkl}} \quad (2)$$

where  $\lambda$  and  $\theta_{hkl}$  are the wavelength of the used x-ray and diffraction angle, respectively. The calculated values for the samples U900 and N500-180 are given in Table 2. As can be seen, the nitriding leads to the meaningful dimensional variations in  $a$ ,  $b$ , and directions. While the AT unit cell undergoes an insignificant expansion in  $a$  (about 0.9%) and  $b$  (about 1.01%) directions, it is considerably compressed in  $c$  direction (around 1.34%). This strain can be attributed to the incorporation of nitrogen atoms into the AT lattice structure.

From the macroscopic point of view, the sample U900 bears a white appearance, but at the nitrated samples, the higher the doped nitrogen content, the larger the population of gray particles appears (see Fig. 5c). A careful look at the nitrated samples confirms the presence of some black particles being uniformly distributed inside the powdery samples of lower photodegradation efficiency (see Fig. 5c). As seen, the appearance of the black particles is entirely different from that of white/gray particles and their nitrogen content transcends white/gray particles. The EDS analysis proves that the nitrogen-rich particles have more than 10 wt% of nitrogen, i.e. several times higher than white or gray powdery samples. It can be concluded that the different contents of diffused nitrogen atoms in the particles may lead to a broad spectrum of colors from white to gray one.

**3.1.2.2. TEM analysis.** More investigations are required to characterize the black particles by TEM observations. Fig. 6 shows HRTEM images of the black particles present in the sample N500-60 benefiting from 3.5 wt% of nitrogen. As seen, there is a limited population of black nanoparticles appearing as dark regions. These regions include a sporadic distribution of dark points as a representative of nitrogen-rich atomic sites or point defects. More importantly, these points are often accumulated at the superficial regions of black particles (see red arrows in Fig. 6c), as well as uniformly dispersed in particles interiors (see yellow arrows in Fig. 6c). It implicitly shows that a vast majority of nitrogen atoms are absorbed on the surface and less content is penetrated into the interior regions. The interplanar distance estimated by the TEM observations at higher magnifications is about 0.33 nm for the as-received AT particles. This value is equal to the standard “d” value of (022) plane in  $Al_2TiO_5$  [40].

**3.1.2.3. XPS analysis.** XPS analysis was carried out to examine whether the nitrogen atoms are successfully doped into the lattice structures of  $TiO_2$ ,  $Al_2O_3$ , and  $Al_2TiO_5$  phases and to survey the chemical status of involved elements. As given in Fig. 7, the XPS spectrum confirms the existence of Al, O, N, Ti, and C elements in all nitrated samples. The binding energies were calibrated by taking the carbon  $C_{1s}$  peak (284.6 eV) as the reference [41]. Fig. 7a

shows the high-resolution XPS spectra of the  $O_{1s}$  peak for the samples U900, N300-30, and N500-30, ranging between 528.1 and 534 eV. The  $O_{1s}$  peak in all three samples can be deconvoluted to two distinct peaks. These peaks are centered at 530.2 eV and 531.3 eV for U900. While the first peak can be attributed to the crystal lattice oxygen [42,43], the second one can be related to the presence of O-H groups on the surface of the particles [41,44–46]. On the other hand, the  $O_{1s}$  peaks have been partially shifted to lower binding energies in N300-30 and to higher ones in N500-30. It confirms the formation of oxygen vacancies in N300-30, which is consistent with improved photodegradation results [47–50].

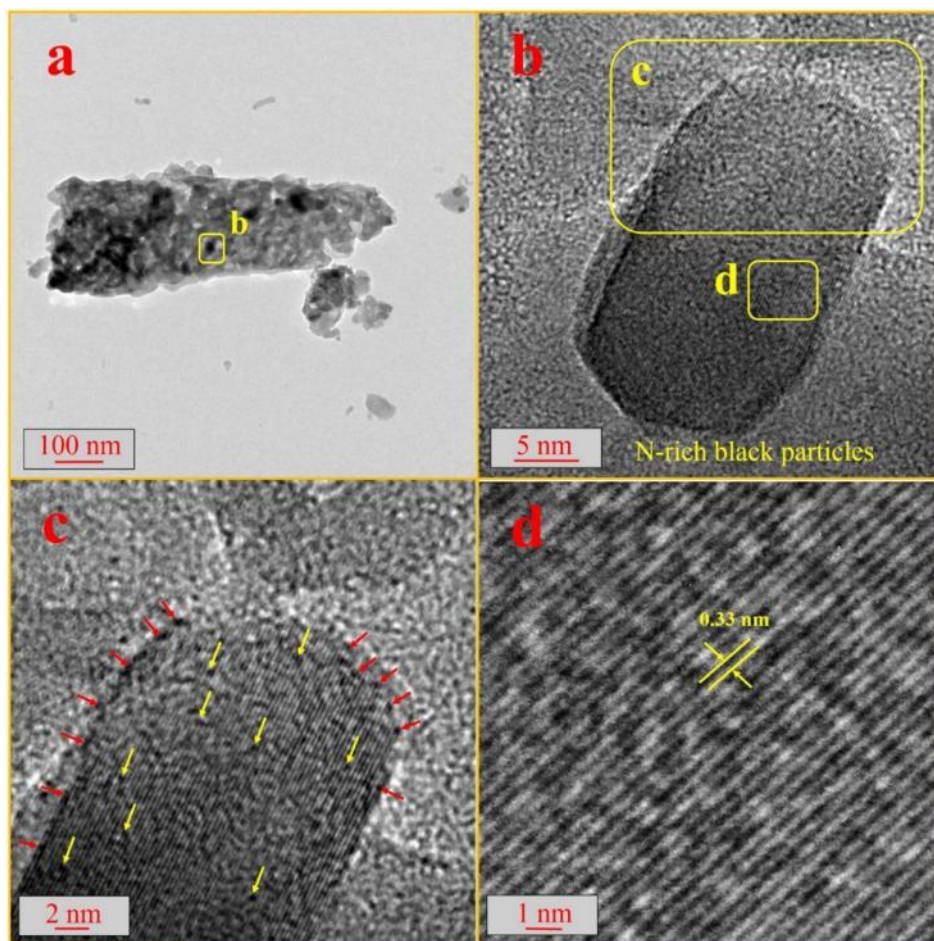
Fig. 7b shows the high-resolution XPS spectra of the  $Al_{2p}$  peak for the samples U900, N300-30, and N500-30, ranging between 72 and 76 eV. This broad peak can be fitted with two Gaussian components. The first component for U900 is centered at 73.7 eV and can be attributed to the presence of Al-metal (i.e. Al-Ti) bonds in the  $Al_2TiO_5$  phase [51]. Besides, the second component falls into 74.3 eV and may be assigned to the presence of  $Al^{3+}$  ions in the form of aluminum oxide ( $Al_2O_3$ ) and/or aluminum hydroxides (i.e.  $AlO(OH)$  and  $Al(OH)_3$ ) [51–54]. Typically, it is difficult to discern which chemical form (i.e. oxide or hydroxide) is preferred by the  $Al^{3+}$  ions based on the  $Al_{2p}$  peak alone. One approach to distinguish the formed species is to determine the range in which the  $O_{1s}$  peak emerges. If the  $O_{1s}$  peak falls into high binding energies (almost 532.8 eV), the possible phase is aluminum hydroxide, but if it is centered at 531.3 eV, the  $Al^{3+}$  ions tend to form aluminum oxide. Since the  $O_{1s}$  peak in the present work is centered at 531.3 eV, the existence of  $Al_2O_3$  phase is confirmed [51]. As a significant clue, the intensity of the first peak is higher than that of the second one, which confirms the abundance of the  $Al_2TiO_5$  phase rather than  $Al_2O_3$ .

Fig. 7c indicates the high-resolution XPS spectra of two distinct  $Ti_{2p}$  peaks for the samples U900, N300-30, and N500-30, ranging between 456 and 467 eV. The first peak at 458.7 eV and the second peak at 464.4 eV with a splitting of 5.7 eV correspond to the binding energies of  $Ti_{2p_{1/2}}$  and  $Ti_{2p_{3/2}}$ , respectively. The existence of these peaks indicates that Ti exists in the form of  $Ti^{4+}$  ions in  $TiO_2$  and  $Al_2TiO_5$  [49,55–57].

Fig. 7d shows the high-resolution XPS spectra of the  $N_{1s}$  peak for the samples U900, N300-30, and N500-30, ranging between 398 and 403 eV. As seen, after the deconvolution, several peaks emerged. For the sample N300-30, the peaks were centered at 399.2, 400.4, 401.2, and 402 eV, respectively. As the literature have reported, the first peak at 399.2 eV may be attributed to the existence of tertiary pyrrolic nitrogen ( $N-C_3$ ) [58,59]. The second peak at 400.4 eV can be assigned to the formation of O-Ti-N linkages by interstitial nitrogen atoms [42,57,60]. The third peak at 401.2 eV corresponds to the quaternary nitrogen attached to three carbon atoms in the aromatic cycles [61] and the absorption of  $NH_4^+$  cations to  $Ti-O^-$  sites (i.e. Ti-O-N bonds) [62]. Finally, the fourth peak centered at 402 eV may be attributed to the presence of molecularly adsorbed nitrogen species such as N-O, N-N, and N-H [46]. These four peaks indicate that the nitrogen atoms are successfully penetrated into interstitial sites of the crystal lattices

**Table 2**  
Quantitative analysis of XRD patterns for the samples U900 and N500-180.

Sample	2 $\theta$ (Degree)	Diffraction plane	d spacing ( $\text{\AA}$ )	Lattice constant ( $\text{\AA}$ )
U900	19.121	(020)	4.6382	a = 3.6646, b = 9.2764, c = 9.6971
U900	26.578	(022)	3.3516	
U900	27.721	(111)	3.2155	
N500-30	18.942	(020)	4.6852	a = 3.6978, b = 9.3704, c = 9.5672
N500-30	26.612	(022)	3.3472	
N500-30	27.534	(111)	3.2368	



**Fig. 6.** HRTEM images of black particles in the sample N500-60 in different magnifications. The yellow and red arrows indicate the atomic sites in which nitrogen is accumulated during the nitriding treatment. (For interpretation of the references to colour in this figure legend, the reader is referred to the web version of this article.)

in N300-30. Conversely, for the sample N500-30, the peaks are centered at 398.8, 400.4, and 401.6 eV, respectively. The first peak at 398.8 eV can be assigned to the existence of  $sp^2$  hybridized nitrogen atom in the triazine rings ( $C-N=C$ ) [63] and the generation of O-Ti-N bonds owing to the substitution of O atoms by nitrogen ones [43]. The second peak at 400.4 eV may be attributed to the formation of O-Ti-N linkages by interstitial nitrogen atoms [42,57,60] and the existence of tertiary pyrrolic nitrogen ( $N-C_3$ ) [58,59]. Finally, the third peak at 401.6 eV may be ascribed to the attachment of nitrogen species at superficial oxygen sites such as  $NO_x$  [58]. These three peaks prove that the nitrogen atoms are successfully penetrated into both interstitial and substitutional sites of the crystal lattices in N300-30.

**3.1.2.4. FTIR analysis.** The FTIR spectroscopy of the AT-based nanostructure before and after the nitriding was carried out to provide more details about their structure and existing chemical linkages. Fig. 8 indicates the FTIR spectra of the samples, where the broad adsorption peaks at around  $3400\text{ cm}^{-1}$  and  $1630\text{ cm}^{-1}$  emerge. These peaks can be attributed to the surface hydroxyl groups or chemisorbed water molecules [64–66]. There is also another peak near around  $1023\text{ cm}^{-1}$  which can be assigned to the OH bending mode [40]. There are also two adsorption bands between 700 and  $900\text{ cm}^{-1}$  which are the characteristic modes of the AT crystal structure. While the peak around  $730\text{--}740\text{ cm}^{-1}$  may be ascribed to the Al-O stretching vibration in octahedral  $AlO_6$  units [67,68], the peak centered at  $870\text{ cm}^{-1}$  appears due to the Ti-O bending

modes in  $TiO_6$  units [5–6]. The emergence of some adsorption bands near around  $1460\text{ cm}^{-1}$  and  $1250\text{ cm}^{-1}$  at the FTIR spectra of the annealed samples indicates that the nitrogen atoms are embedded in AT and  $TiO_2$  lattice structures. Also, the nitriding process results in the formation of NO-like species such as  $N_2O_2^{-2}$  and  $NO^{-1}$  (centered at  $1380\text{--}1390\text{ cm}^{-1}$  and  $1105\text{--}1110.1\text{ cm}^{-1}$ , respectively). This finding confirms the XPS results [64,66].

## 3.2. Optical characterization

### 3.2.1. Photocatalytic activity measurement

The photodegradation of MB under the UVa irradiation was measured to elucidate how the thermal annealing of the AT-based nanostructure in the nitrogen atmosphere can influence their photocatalytic performance. The characteristic peak at 664 nm was used to determine the remaining MB concentration at solution. In the absence of the photocatalyst, no significant change was observed in MB concentration after a 2-hour illumination. As exemplary cases, Fig. 9(a-b) shows the absorbance spectra of MB for the samples N400-30 and U900. As shown, the peak intensity of MB decreases gradually in the presence of the AT photocatalyst, as the photodegradation proceeds.

Fig. 9c indicates the photocatalytic degradation of all nitrided samples versus time. As clearly seen, for the sample N400-30, the photodegradation of MB dye reaches 56% after 120 min under UVa, i.e. about 1.4 times higher than that measured for the sample U900. This value was the maximum degradation between all the

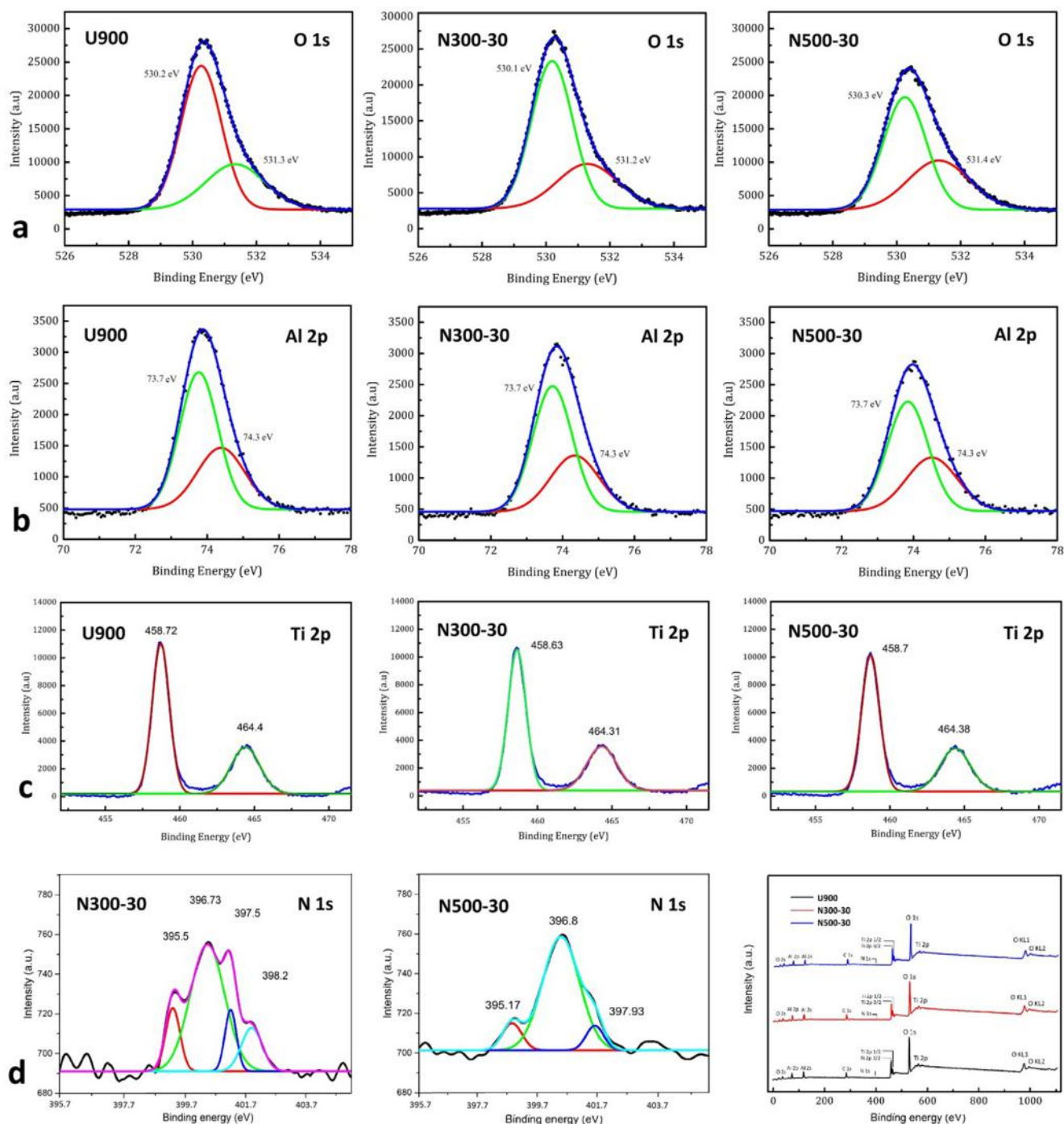


Fig. 7. High-resolution XPS spectra of (a) O 1s, (b) Al 2p, (c) Ti 2p, (d) C 1s, and (e) N 1s for the samples U900, N300-30, and N500-30.

samples. In contrast, only 28% of MB dye was degraded in the presence of the sample N300-60, which is the highest diminution in the photoactivity among the samples. Table 3 presents a brief list of the photocatalytic efficiency of all samples. After the sample N400-30, the specimens N300-30 and N400-180 show highest photocatalytic performance with respect to the sample U900 after the exposure to the UV irradiation for 120 min.

For all nitrated samples, a similar trend was observed for the variation of photocatalytic activity against the nitrating time at all annealing temperatures: the photocatalytic activity first decreases by extending the annealing time from 30 min to 1 h, reaches a minimum, and then increases from 1 h to

3 h. It is while the nitrogen content of the samples increases from 30 min to 1 h, reaches a maximum, and then decreases from 1 to 3 h. At all three temperatures, minimum MB degradation is associated with the samples annealed for 1 h and filled with the highest nitrogen content. This fact indicates that the content of doped nitrogen is the major factor affecting the photocatalytic performance of the samples at a constant temperature.

Since the initial amount of MB is exceedingly low, it was assumed that the heterogeneous dye photodegradation reaction follows a pseudo first-order equation according to the Langmuir-Hinshelwood kinetic model as follows [69–71]:

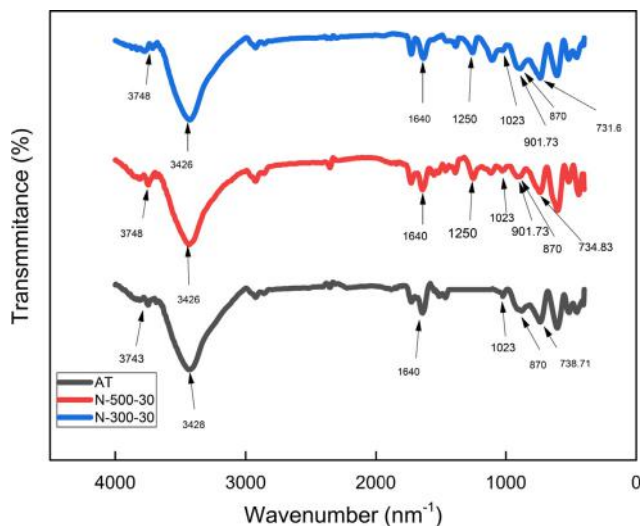


Fig. 8. FTIR spectra of the samples U900, N300-30 and N500-30.

$$\ln(C/C_0) = kt \quad (3)$$

where  $C_0$  is the initial MB concentration,  $C$  is the remaining MB concentration at an arbitrary reaction time  $t$ , and  $k$  is the apparent rate constant which quantifies the rate of photodegradation process. The higher the  $k$  value, the faster the photodegradation process is. To determine the value  $k$ ,  $\ln(C/C_0)$  needs to be plotted versus time, and the gradient of the fitted trendline is calculated. Fig. 9d and Table 3 present the kinetic plots of all nitrided samples and calculated reaction constants ( $k$ ) for different samples. As obviously seen, the sample N400-30 bears the maximum  $k$  value (i.e.  $0.0068 \text{ min}^{-1}$ ), which is about 1.8 times higher than that of U900 (i.e.  $0.0038 \text{ min}^{-1}$ ). In contrast, the sample N300-60 has the minimum value  $k$  (i.e.  $0.0030 \text{ min}^{-1}$ ) which is 21% smaller than that of U900. Fig. 9e indicates the variation of  $k$  values versus the annealing time at different temperatures. As seen, the constant  $k$  first decreases by extending the annealing time from 30 min to 1 h, reaches a minimum, and then increases from 1 to 3 h. This trend is in good agreement with ones observed for the dye degradation efficiency.

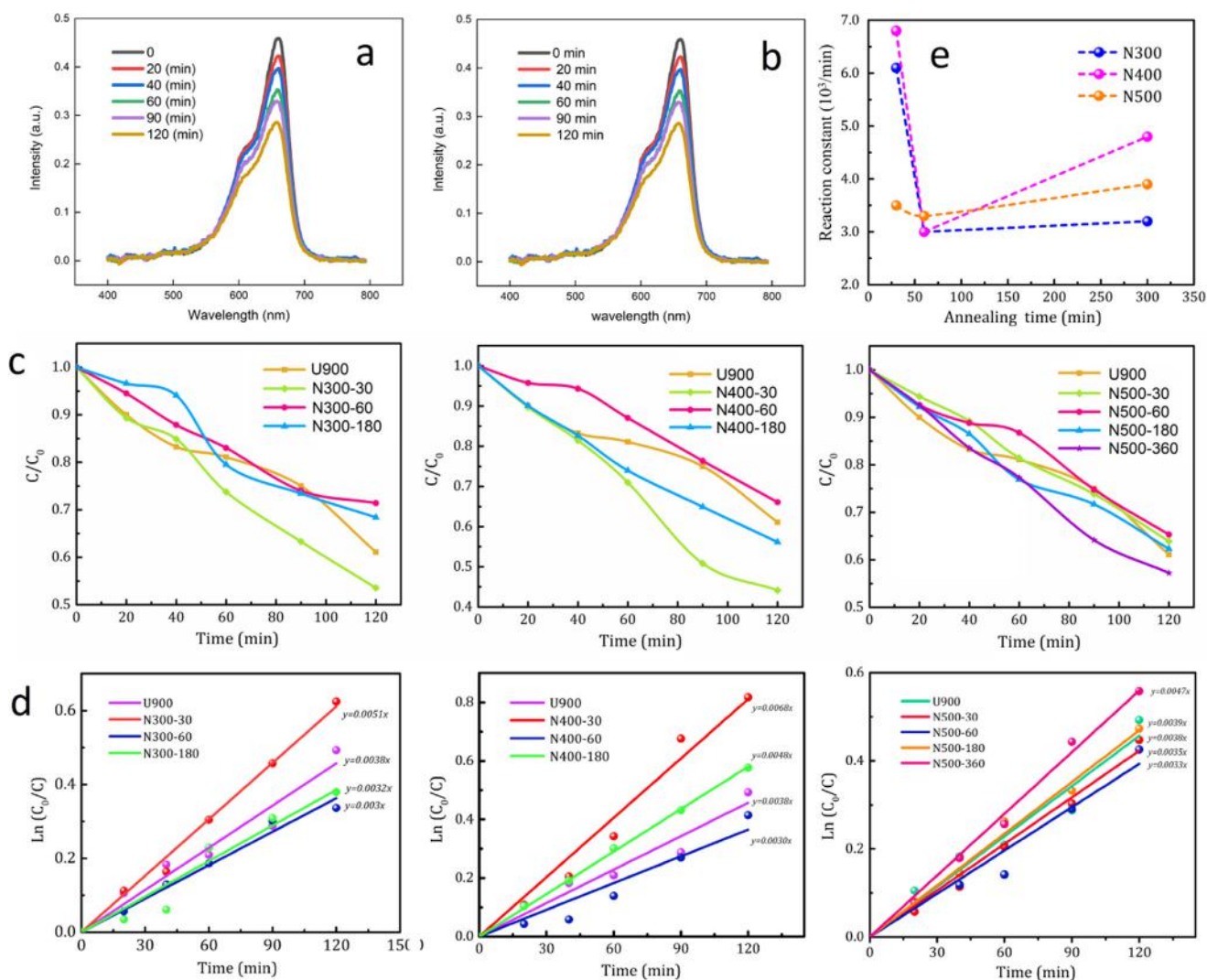


Fig. 9. (a) Absorbance spectra of MB in the presence of the sample N400-30 and (b) U900; (c) Photocatalytic degradation of MB-containing solution by using different AT-based nanostructures annealed at 300, 400 and 500 °C; (d) Kinetic plots of different samples nitrided at 300, 400, and 500 °C; (e) The variation of apparent rate constant ( $k$ ) as a function of annealing time at different nitriding temperatures.

**Table 3**

The kinetic evaluation of nitrated samples including the degradation efficiency, relative photocatalytic alterations after nitrating, and related reaction constants.

Sample	Degradation efficiency after 120 min	Relative photocatalytic variations (%)	K value ( $\text{min}^{-1}$ )
U900	38.9	–	0.0038
N300-30	46.5	+19.5	0.0051
N300-1	28.6	–26.4	0.0030
N300-3	31.6	–18.7	0.0032
N400-30	55.9	+43.7	0.0068
N400-1	33.9	–12.8	0.0030
N400-3	43.9	+12.8	0.0048
N500-30	36.1	–7.2	0.0035
N500-1	34.7	–10.8	0.0033
N500-3	37.7	–3.1	0.0039

### 3.2.2. Recyclability test

The stability of the doped photocatalyst is a critical factor for a long time. To evaluate this property, the recycling experiment was carried out for 5 runs by the powder separation and subsequent photocatalytic test for consecutive cycles. The obtained results are given in Fig. 10. As can be seen, the photocatalytic degradation efficiency of the sample N400-30 decreased from 55.9% to 47.71% after 5 runs. Therefore, only 14.6% decline in the photocatalytic performance was observed, which indicates that the photocatalyst still exhibits a desirable stability and durability after 6 runs.

### 3.2.3. PL analysis

Albeit the band gap narrowing (or widening) may increase (or decrease) the material capability to absorb the incident photon and generate electron-hole pairs [72], it does not guarantee a significant increment (or decrement) in the photocatalytic activity [73]. To benefit from the better photocatalytic activity, the photo-generated electron-hole pairs need to be efficiently separated, successfully transferred through the material, and ultimately gotten involved in the photocatalytic reactions at the surface of target semiconductor [74]. The recombination decreases the population of accessible charge carriers [75]. To study the recombination probability of the photo-generated electron-hole pairs in the samples, the photoluminescence (PL) emission spectroscopy is a robust tool. Fig. 11a shows the PL spectrum of the samples with excitation at 355 nm at room temperature. As seen, the PL signal intensities of

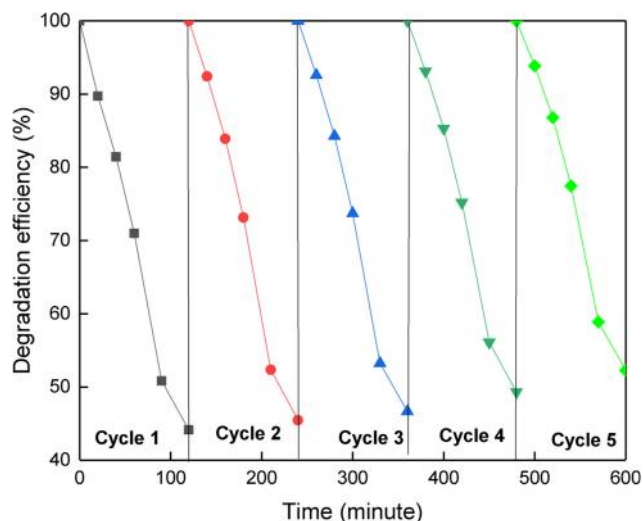


**Fig. 10.** Photocatalytic degradation of MB-containing solution by the sample N400-30 after five subsequent cycles.

the specimens are to some extent consistent with the trend of photocatalytic activity of the samples (i.e. N400-60 > N500-30 > U900 > N300-30). The weaker the recorded signal, the lower the recombination of photo-induced charges. Therefore, for the samples N500-30 and N300-30, the incorporation of the nitrogen atoms into the AT lattice is accompanied by declining the recombination centers of the electron-hole pairs. However, for the case of N400-60, the additional treatment facilitates the recombination process. It is worth mentioning that the lower recombination of photo-induced charges may arise from the lower density of photo-induced electron-hole pairs ab initio. This fact may be attributed to the weak capability of the matter in generating the electron-hole pairs under the irradiation [73,75,76]. It seems that further studies should be performed to unveil the reason behind the variation of PI intensities for the nitrated samples.

### 3.2.4. DRS analysis

As a standard technique, UV-vis DRS is usually used to study the light adsorption properties of solid materials. The experimental data obtained from the DRS measurements can be beneficial to evaluate the optical band gap of the target samples [77]. Fig. 11b indicates the DRS spectra of U900 and nitrated specimens. Using the DRS data, tauc plots can be obtained by plotting the term  $(\alpha h\nu)^n$  as a function of incident photon energy  $h\nu$  (according to Eq. (4):

$$(\alpha h\nu)^n = A(h\nu - E_g) \quad (4)$$

where  $\alpha$ ,  $\nu$ ,  $h$ ,  $E_g$ , and  $A$  are the adsorption coefficient, light frequency, Planck's constant, band gap energy, and a constant, respectively. The parameter "n" is a factor corresponding to the electronic transitions so that if  $n = 0.5$ , the semiconductor bears an indirect transition, but  $n = 2$  is for a direct transition. The band gap of the material can be estimated by the extrapolation of the linear region observed in the tauc plot [78,79]. Fig. 11c indicates the tauc plots of the samples. The calculated band gap values were 2.73, 2.78, 2.88 and 2.9 eV for N300-30, N500-30, U900, and N400-1, respectively. It means that the  $N_2$  treatment may lead to the bandgap narrowing of the samples N300-30 and N500-30. However, the band gap value of the sample N400-60 is found to be slightly higher than that of U900. This fact may be ascribed to the Burstein-Moss effect. At the higher contents of the dopant material, the excess charge carriers occupy the lower states of the conduction band, thereby pushing the Fermi energy level of the semiconductor into the energy zone of the conduction band. According to the Pauli Exclusion Principle, the occupied energy states are forbidden from the optical or thermal transitions to these states. It means that only the states with the energy levels beyond the Fermi energy are available for the electron transitions from the valence band to these states. Therefore, to make these transitions happen, it is needed to provide photons with the energy content higher than the intrinsic band gap of the semiconductor. Consequently, the calculated band gap energy from DRS is slightly shifted to higher energy values [80,81].

Accordingly, one can determine the band edge positions of the valence band (VB) and conduction band (CB) of the samples by the Mulliken electronegativity theory [82,83] as follows:

$$E_{VB} = \chi - E_C + 0.5E_g$$

$$E_{CB} = E_{VB} - E_g \quad (5)$$

where  $\chi$  is the absolute electronegativity of the material and can be determined by the geometric average of the atoms.  $E_C$  is also the energy of free electrons vs. the normal hydrogen electrode (i.e. 4.5 eV). Table 4 shows the estimated  $E_g$ ,  $E_{VB}$ , and  $E_{CB}$  values for the samples.

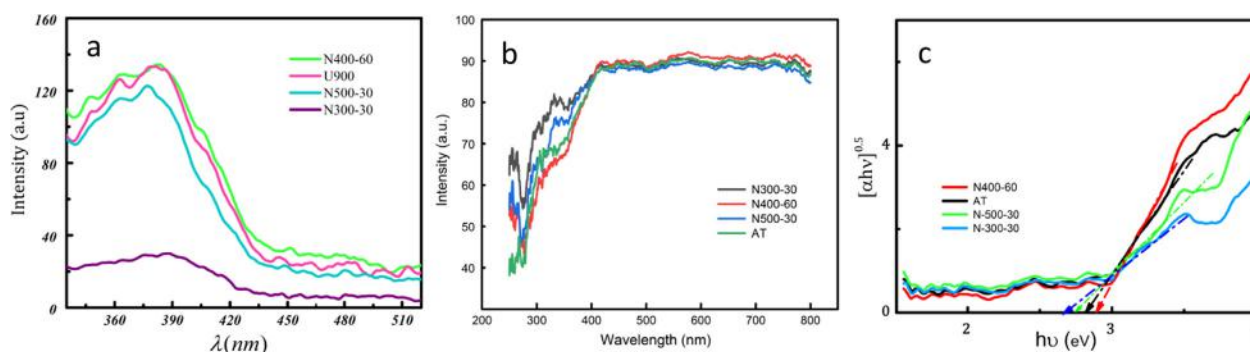


**Fig. 11.** (a) PI spectra of the samples U900, N400-60, N300-30, and N500-30; (b) DRS spectra of the samples U900, N400-60, N300-30, and N500-30, and (c) their corresponding tauc plots.

### 3.3. Photoelectrochemical characterization

#### 3.3.1. EIS analysis

To further study the correlation between the annealing in  $N_2$  atmosphere and photoresponse of the AT-based nanostructure, the transferability of charge carriers must be determined [84,85]. For this purpose, the electrochemical impedance spectroscopy (EIS) measurements were performed, and corresponding EIS Nyquist plots of the samples were plotted in Fig. 12a. This plot indicates the imaginary impedance component ( $Z''$ ) against the real impedance component ( $Z'$ ). The obtained semi-circle curve is related to the faradic process originating from the presence of electron-transfer limiting steps. Typically, in higher frequencies, the smaller diameter of the semi-circle Nyquist curve can be attributed to better charge transportability [86,87]. Fig. 12a shows that the semi-circle curve of the nitrated samples is smaller than that of the sample U900. This fact points out that the annealing process diminishes the catalyst/electrolyte interface charge resistance and improves the charge transfer rate which finally results in efficient electron-hole separation.

#### 3.3.2. Photocurrent measurements

To further shed light on the charge transport characteristics of non-doped and n-doped AT-based heterostructures, the photocurrent generation of the samples U900, N300-30, and N500-30 were performed under the UVA irradiation. The results are given in Fig. 11(b-c). Quantitatively, the potential collected with reference electrode to the Ag/AgCl electrode must be converted to the reversible hydrogen electrode according to Eq. (6):

$$E_{\text{RHE}} = E_{\text{Ag/AgCl}} + 0.059\text{pH} + E_{\text{Ag/AgCl}}^0 \quad (6)$$

where  $E_{\text{Ag/AgCl}}$  is the working potential and  $E_{\text{Ag/AgCl}}^0$  is 0.1976 V at 25 °C. The results are given in Fig. 12(b-c). As seen in Fig. 12b, a gradual increment in the applied potential can continuously increase the total density of photogenerated charge carriers in all three samples. This effect indicates that all the samples behave similar to an n-type

semiconductor [88,89]. On the other hand, the photocurrent density of the sample N300-30 is higher than that of N500-30 and U900 at all potentials, suggesting the lowest recombination and highest photogeneration capacity [90,91]. As an interesting fact, the n-doping in N300-30 can successfully shift the minimum potential at which the photocatalyst begins to produce the photocurrent (i.e. threshold potential) to lower potential levels with respect to U900 and N500-3. It means that the photocurrent of a certain intensity can be generated under lower potential levels, implicitly proving the acceleration of photogenerated charge carriers through the nitrogen penetration into the AT-based heterostructure. The calculated photocurrent density for the specimens U900, N500-3, and N300-30 are 1.9, 3.04, and 5.6  $\mu\text{A}/\text{cm}^2$ , respectively.

At 1.2 V, the photocurrent intensity of the sample N300-30 increases by a factor of 1.6 and 2.4 with respect to U900 and N500-30, respectively. These factors increase up to 1.7 and 2.7 at the potential level of 1.6 V. In contrast, the difference between the photocurrents below 0.8 V is ignorable for three samples. The most determining factor in the photocurrent intensity at relatively low potential levels is the electron-hole recombination. The identical photocurrent intensities at low applied potentials confirm that the recombination is wholly independent of the nitrogen doping nature. It is while at high applied potentials, the predominant factor is the activation of superficial catalytic reactions in the particles rather than the recombination degree. Therefore, the higher photocurrent intensity of the sample N300-30 at high potentials can be attributed to its more active surface catalytic reactions and lower charge carrier recombination, compared to U900 and N500-30 [91].

Fig. 12c shows the current density-potential curves of the samples U900, N300-30, and N500-30 under the chopped UVA illumination. The photocurrent is the difference between the current intensity when the UVA irradiation is on and off [89]. As seen, both non-doped and n-doped samples are capable of generating the photocurrent, but the sample N300-30 is more successful than U900 and N500-30 because the photocurrent intensity of N300-30 is about twice as high as U500-30. Also, all the specimens indicate the significant dark current, providing evidence for this fact that both non-doped and n-doped samples exhibit the electrocatalytic behavior in addition to the photocatalytic one [92]. As the main conclusion, the charge separation and transport in the sample N300-30 are more efficient than U900 and N500-30, because the higher the photocurrent density, the faster the charge carrier transport and more suppressed the recombination [92]. The results are consistent with the photodegradation and PI tests, where the sample N300-30 exhibits higher dye degradation than the samples U900 and N500-30 and the recombination rate is lower than others.

**Table 4**

The calculated  $E_g$ ,  $E_{\text{VB}}$ , and  $E_{\text{CB}}$  values for the samples U900, N300-30, N500-30, and N400-60.

Sample	$E_g$	$E_{\text{VB}}$	$E_{\text{CB}}$
N300-30	2.73 eV	2.397 eV	-0.333 eV
N500-30	2.78 eV	2.422 eV	-0.358 eV
U900	2.88 eV	2.472 eV	-0.408 eV
N400-60	2.9 eV	2.482 eV	-0.418 eV

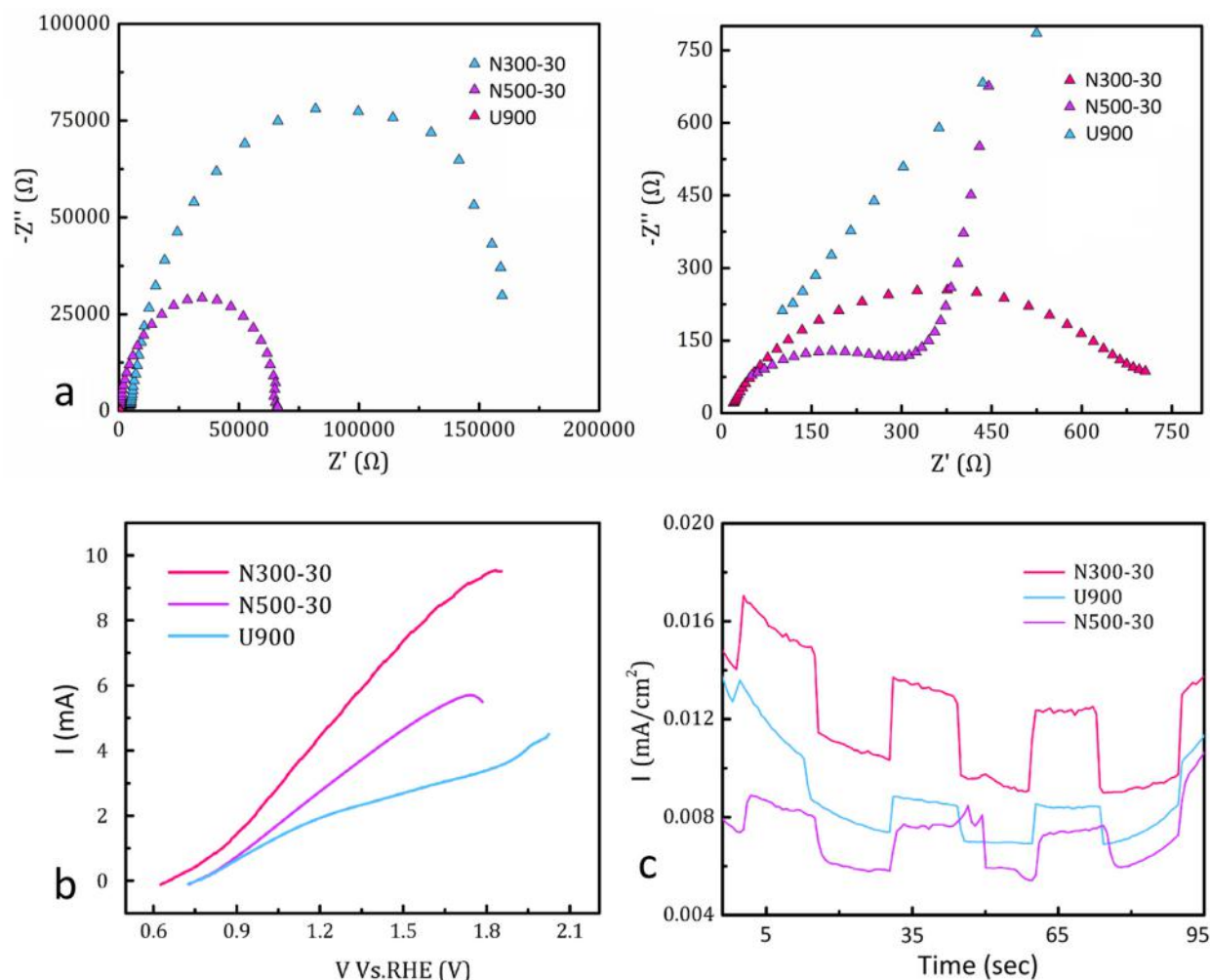


Fig. 12. (a) EIS Nyquist plots of the samples U900, N300-30 and N500-30 at different magnifications; (b) Current vs applied potential curves for the samples U900, N300-30 and N500-30 under UVA; and (c) Photocurrent plots of N300-30, N500-30 and U900 under UVA irradiation with a certain on-off period.

#### 4. Conclusions

A hybrid aluminium titanate ( $\text{Al}_2\text{TiO}_5$ )-based heterostructure was synthesized by the citrate sol-gel method and exposed to a continuous flow of the nitrogen gas to tailor its band structure and electronic response through the n-doping and generation of surface oxygen vacancies. A variety of characterization techniques were used to determine the energy level of valence/conduction bands, band gap width, electron-hole separation and recombination rate, and intrinsic resistance of the semiconductor against the electron-hole transport. The most important results are given as follows:

- The synthesized semiconductor is composed of three main constituents, i.e.  $\text{Al}_2\text{TiO}_5$  as the dominant phase, and  $\text{Al}_2\text{O}_3$  and  $\text{TiO}_2$  as the minor ones. These phases bear an average size of 50 nm with a weak bond to neighboring units.
- A limited population of ubiquitous microcracks was propagated during the nitriding due to the thermal anisotropy of the AT ceramic during the cooling step and evolution of residual stresses as a consequence of diffusing nitrogen atoms into the AT crystal structure.
- The nitriding can change the electronic structure of these phases relative to each other, controlling their photocatalytic performance. It was indicated that the nitrogen doping could

not improve the photocatalytic performance of the semiconductor in all nitriding time and temperature conditions. Any variation in the photogeneration behavior of the samples was attributed to the formation of some new bonds in the crystal structure (including O-Ti-N and Ti-N), the substitutional or interstitial replacement of nitrogen atoms with oxygen atoms, molecular chemisorption of nitrogen, and the attachment of nitrogen species at superficial oxygen sites.

- The formation of new bonds varies the bandgap values from 2.88 eV for pristine AT to 2.73 eV for the nitrided one, thereby manipulating the charge carrier recombination rate and activation of superficial catalytic reactions in the particles.
- Numerically, it was shown that the band structure variations can efficiently increase the photodegradation efficiency of methylene blue and apparent rate constant ( $k$ ) by 1.4 times (from 38.9 to 55.9%) and 1.8 times (from 0.0038 to 0.0068  $\text{min}^{-1}$ ).

#### References

- [1] I. Zama, C. Martelli, G. Gorni, Preparation of  $\text{TiO}_2$  paste starting from organic colloidal suspension for semi-transparent DSSC photo-anode application, *Mater. Sci. Semicond. Process.* 61 (2017) 137–144.
- [2] G.-Q. Ma, F.-S. Liu, S. Wang, Z.-C. Dang, J.-W. Zhang, X.-J. Fu, M.-S. Hou, Preparation and characterization of  $\text{Bi}_2\text{S}_3/3\text{DOM-TiO}_2$  for efficient

- photocatalytic degradation of rhodamine B, *Mater. Sci. Semicond. Process.* 100 (2019) 61–72.
- [3] L. Muñoz-Fernandez, A. Sierra-Fernández, G. Flores-Carrasco, O. Milošević, M.E. Rabanal, Solvothermal synthesis of Ag/ZnO micro/nanostructures with different precursors for advanced photocatalytic applications, *Adv. Powder Technol.* 28 (2017) 83–92.
  - [4] K. Intarasuwan, P. Amornpitoksuk, S. Suwanboon, P. Graidist, S. Maungchanburi, C. Random, Effect of Ag loading on activated carbon doped ZnO for bisphenol A degradation under visible light, *Adv. Powder Technol.* 29 (2018) 2608–2615.
  - [5] S. Adhikari, K.S. Chandra, D.-H. Kim, G. Madras, D. Sarkar, Understanding the morphological effects of WO<sub>3</sub> photocatalysts for the degradation of organic pollutants, *Adv. Powder Technol.* 29 (2018) 1591–1600.
  - [6] X. Wang, H. Fan, P. Ren, Effects of exposed facets on photocatalytic properties of WO<sub>3</sub>, *Adv. Powder Technol.* 28 (2017) 2549–2555.
  - [7] Y. Deng, L. Tang, C. Feng, G. Zeng, Z. Chen, J. Wang, H. Feng, B. Peng, Y. Liu, Y. Zhou, Insight into the dual-channel charge-carrier transfer path for nonmetal plasmonic tungsten oxide based composites with boosted photocatalytic activity under full-spectrum light, *Appl. Catal., B* 235 (2018) 225–237.
  - [8] A. Biswas, A. Chakraborty, N.R. Jana, Nitrogen and Fluorine Codoped, Colloidal TiO<sub>2</sub> Nanoparticle: Tunable Doping, Large Red-Shifted Band Edge, Visible Light Induced Photocatalysis, and Cell Death, *ACS Appl. Mater. Interfaces* 10 (2018) 1976–1986.
  - [9] J. Schneider, D. Bahnemann, J. Ye, G.L. Puma, D.D. Dionysiou, Photocatalysis: fundamentals and perspectives, *R. Soc. Chem.*, 2016.
  - [10] M. Behpour, R. Foulady-Dehaghi, N. Mir, Considering photocatalytic activity of N/F/S-doped TiO<sub>2</sub> thin films in degradation of textile waste under visible and sunlight irradiation, *Sol. Energy* 158 (2017) 636–643.
  - [11] J. Zhang, B. Wu, L. Huang, P. Liu, X. Wang, Z. Lu, G. Xu, E. Zhang, H. Wang, Z. Kong, Anatase nano-TiO<sub>2</sub> with exposed curved surface for high photocatalytic activity, *J. Alloys Compd.* 661 (2016) 441–447.
  - [12] Z. Hu, J. Lyu, M. Ge, Role of reactive oxygen species in the photocatalytic degradation of methyl orange and tetracycline by Ag<sub>3</sub>PO<sub>4</sub> polyhedron modified with g-C<sub>3</sub>N<sub>4</sub>, *Mater. Sci. Semicond. Process.* 105 (2020) 104731.
  - [13] Y. Guo, P. Wang, J. Qian, Y. Ao, C. Wang, J. Hou, Phosphate group grafted twinned BiPO<sub>4</sub> with significantly enhanced photocatalytic activity: Synergistic effect of improved charge separation efficiency and redox ability, *Appl. Catal., B* 234 (2018) 90–99.
  - [14] F. Bakhshandeh, A. Azarniya, H.R.M. Hosseini, S. Jafari, Are aluminium titanate-based nanostructures new photocatalytic materials? Possibilities and perspectives, *J. Photochem. Photobiol., A* 353 (2018) 316–324.
  - [15] T. Wang, B.R. Li, L.G. Wu, Y.B. Yin, B.Q. Jiang, J.Q. Lou, Enhanced performance of TiO<sub>2</sub>/reduced graphene oxide doped by rare-earth ions for degrading phenol in seawater excited by weak visible light, *Adv. Powder Technol.* 30 (2019) 1920–1931.
  - [16] Q. Wu, Z. Zhang, The preparation of self-floating Sm/N co-doped TiO<sub>2</sub>/diatomite hybrid pellet with enhanced visible-light-responsive photoactivity and reusability, *Adv. Powder Technol.* 30 (2019) 415–422.
  - [17] T. Choi, J.-S. Kim, J.H. Kim, Transparent nitrogen doped TiO<sub>2</sub>/WO<sub>3</sub> composite films for self-cleaning glass applications with improved photodegradation activity, *Adv. Powder Technol.* 27 (2016) 347–353.
  - [18] A. Eshaghi, H. Moradi, Optical and photocatalytic properties of the Fe-doped TiO<sub>2</sub> nanoparticles loaded on the activated carbon, *Adv. Powder Technol.* 29 (2018) 1879–1885.
  - [19] B. Ahmmad, Y. Kusumoto, M.S. Islam, One-step and large scale synthesis of non-metal doped TiO<sub>2</sub> submicrospheres and their photocatalytic activity, *Adv. Powder Technol.* 21 (2010) 292–297.
  - [20] J.Y. Kim, C.S. Kim, H.K. Chang, T.O. Kim, Synthesis and characterization of N-doped TiO<sub>2</sub>/ZrO<sub>2</sub> visible light photocatalysts, *Adv. Powder Technol.* 22 (2011) 443–448.
  - [21] J.-A. Cha, S.-H. An, H.-D. Jang, C.-S. Kim, D.-K. Song, T.-O. Kim, Synthesis and photocatalytic activity of N-doped TiO<sub>2</sub>/ZrO<sub>2</sub> visible-light photocatalysts, *Adv. Powder Technol.* 23 (2012) 717–723.
  - [22] Y. Chen, Q. Wu, Q. Jin, K. Liu, A facile sol-gel method for the fabrication of nitrogen doped TiO<sub>2</sub>/NiFe<sub>2</sub>O<sub>4</sub>/diatomite composite with enhanced photoactivity, *Adv. Powder Technol.* 28 (2017) 2225–2231.
  - [23] R. Asahi, T. Morikawa, T. Ohwaki, K. Aoki, Y. Taga, Visible-light photocatalysis in nitrogen-doped titanium oxides, *Sci.* 293 (2001) 269–271.
  - [24] R. Asahi, T. Morikawa, Nitrogen complex species and its chemical nature in TiO<sub>2</sub> for visible-light sensitized photocatalysis, *Chem. Phys.* 339 (2007) 57–63.
  - [25] C. Di Valentin, G. Pacchioni, A. Selloni, S. Livraghi, E. Giamello, Characterization of paramagnetic species in N-doped TiO<sub>2</sub> powders by EPR spectroscopy and DFT calculations, *J. Phys. Chem. B* 109 (2005) 11414–11419.
  - [26] M. Kong, Y. Li, X. Chen, T. Tian, P. Fang, F. Zheng, X. Zhao, Tuning the relative concentration ratio of bulk defects to surface defects in TiO<sub>2</sub> nanocrystals leads to high photocatalytic efficiency, *J. Am. Chem. Soc.* 133 (2011) 16414–16417.
  - [27] J. Fang, H. Fan, Y. Ma, Z. Wang, Q. Chang, Surface defects control for ZnO nanorods synthesized by quenching and their anti-recombination in photocatalysis, *Appl. Surf. Sci.* 332 (2015) 47–54.
  - [28] F. Wang, W. Ge, T. Shen, B. Ye, Z. Fu, Y. Lu, The effect of bulk/surface defects ratio change on the photocatalysis of TiO<sub>2</sub> nanosheet film, *Appl. Surf. Sci.* 410 (2017) 513–518.
  - [29] Y. Chen, Q. Wu, L. Liu, J. Wang, Y. Song, The fabrication of floating Fe/N co-doped titania/diatomite granule catalyst with enhanced photocatalytic efficiency under visible light irradiation, *Adv. Powder Technol.* 30 (2019) 126–135.
  - [30] S. Jeon, C.-J. Choi, T.-Y. Seong, H. Hwang, Electrical characteristics of ZrO<sub>x</sub>N<sub>y</sub> prepared by NH<sub>3</sub> annealing of ZrO<sub>2</sub>, *Appl. Phys. Lett.* 79 (2001) 245–247.
  - [31] B. Kosowska, S. Mozia, A.W. Morawski, B. Grzmil, M. Janus, K. Kałucki, The preparation of TiO<sub>2</sub>-nitrogen doped by calcination of TiO<sub>2</sub>·xH<sub>2</sub>O under ammonia atmosphere for visible light photocatalysis, *Sol. Energy Mater. Sol. Cells* 88 (2005) 269–280.
  - [32] Z. Zhang, X. Wang, J. Long, Q. Gu, Z. Ding, X. Fu, Nitrogen-doped titanium dioxide visible light photocatalyst: spectroscopic identification of photoactive centers, *J. Catal.* 276 (2010) 201–214.
  - [33] C. Fàbrega, T. Andreu, F. Güell, J.D. Prades, S. Estradé, J.M. Rebled, F. Peiró, J.R. Morante, Effectiveness of nitrogen incorporation to enhance the photoelectrochemical activity of nanostructured TiO<sub>2</sub>: NH<sub>3</sub> versus H<sub>2</sub>-N<sub>2</sub> annealing, *Nanotechnol.* 22 (2011) 235403.
  - [34] H. Chen, A. Nambu, W. Wen, J. Graciani, Z. Zhong, J.C. Hanson, E. Fujita, J.A. Rodriguez, Reaction of NH<sub>3</sub> with titania: N-doping of the oxide and TiN formation, *J. Phys. Chem. C* 111 (2007) 1366–1372.
  - [35] A. Sarkar, A. Shchukarev, A.-R. Leino, K. Kordas, J.-P. Mikkola, P.O. Petrov, E.S. Turchina, A.P. Popov, M.E. Darvin, M.C. Meinke, Photocatalytic activity of TiO<sub>2</sub> nanoparticles: effect of thermal annealing under various gaseous atmospheres, *Nanotechnol.* 23 (2012) 475711.
  - [36] X. Fang, Z. Zhang, Q. Chen, H. Ji, X. Gao, Dependence of nitrogen doping on TiO<sub>2</sub> precursor annealed under NH<sub>3</sub> flow, *J. Solid State Chem.* 180 (2007) 1325–1332.
  - [37] A. Azarniya, H.R.M. Hosseini, A new method for fabrication of in situ Al/Al<sub>3</sub>Ti<sub>2</sub>O<sub>3</sub> nanocomposites based on thermal decomposition of nanostructured titanite, *J. Alloys Compd.* 643 (2015) 64–73.
  - [38] A. Azarniya, A. Azarniya, H.R.M. Hosseini, A. Simchi, Nanostructured aluminium titanate (Al<sub>2</sub>TiO<sub>5</sub>) particles and nanofibers: synthesis and mechanism of microstructural evolution, *Mater. Charact.* 103 (2015) 125–132.
  - [39] Negar Keyvani, Abolfazl Azarniya, Hamid Reza Madaah Hosseini, Mohammad Abedi, Dmitry Moskovskikh, Thermal stability and strain sensitivity of nanostructured aluminium titanate (Al<sub>2</sub>TiO<sub>5</sub>), *Mater. Chem. Phys.* 223 (2019) 202–208.
  - [40] M. Sharma, D. Singh, R. Upadhyay, M. Yadav, S. Amritphale, N. Chandra, Novel approach for sol-gel synthesis of nanosize aluminium titanate, *Mater. Res. Innovations* 18 (2014) 235–240.
  - [41] S. Rajoriya, S. Bargoole, S. George, V.K. Saharan, P.R. Gogate, A.B. Pandit, Synthesis and characterization of samarium and nitrogen doped TiO<sub>2</sub> photocatalysts for photo-degradation of 4-acetamidophenol in combination with hydrodynamic and acoustic cavitation, *Sep. Purif. Technol.* 209 (2019) 254–269.
  - [42] T. Suwannaruang, K. Kamonsuangkasem, P. Kidkhunthod, P. Chirawatkul, C. Saiyasombat, N. Chanlek, K. Wantala, Influence of nitrogen content levels on structural properties and photocatalytic activities of nanorice-like N-doped TiO<sub>2</sub> with various calcination temperatures, *Mater. Res. Bull.* 105 (2018) 265–276.
  - [43] K. Kalantari, M. Kalbasi, M. Sohrabi, S.J. Royaei, Enhancing the photocatalytic oxidation of dibenzothiophene using visible light responsive Fe and N co-doped TiO<sub>2</sub> nanoparticles, *Ceram. Int.* 43 (2017) 973–981.
  - [44] Y. Yan, X. Zhou, J. Lan, Z. Li, T. Zheng, W. Cao, N. Zhu, W. Liu, Efficient photocatalytic disinfection of *Escherichia coli* by N-doped TiO<sub>2</sub> coated on coal fly ash cenospheres, *J. Photochem. Photobiol., A* 367 (2018) 355–364.
  - [45] Z. Zhao, T. Kou, L. Zhang, S. Zhai, W. Wang, Y. Wang, Dealloying induced N-doping in spindle-like porous rutile TiO<sub>2</sub> for enhanced visible light photocatalytic activity, *Corros. Sci.* 137 (2018) 204–211.
  - [46] F. Zhou, H. Song, H. Wang, S. Komarneni, C. Yan, N-doped TiO<sub>2</sub>/sepiolite nanocomposites with enhanced visible-light catalysis: Role of N precursors, *Appl. Clay Sci.* 166 (2018) 9–17.
  - [47] C. Liu, L. Zhang, R. Liu, Z. Gao, X. Yang, Z. Tu, F. Yang, Z. Ye, L. Cui, C. Xu, Hydrothermal synthesis of N-doped TiO<sub>2</sub> nanowires and N-doped graphene heterostructures with enhanced photocatalytic properties, *J. Alloys Compd.* 656 (2016) 24–32.
  - [48] D. Zhang, X. Ma, H. Zhang, Y. Liao, Q. Xiang, Enhanced photocatalytic hydrogen evolution activity of carbon and nitrogen self-doped TiO<sub>2</sub> hollow sphere with the creation of oxygen vacancy and Ti<sup>3+</sup>, *Mater. Today Energy* 10 (2018) 132–140.
  - [49] A. Sanchez-Martinez, O. Ceballos-Sanchez, C. Koop-Santa, E.R. López-Mena, E. Orozco-Guareño, M. García-Guaderrama, N-doped TiO<sub>2</sub> nanoparticles obtained by a facile coprecipitation method at low temperature, *Ceram. Int.* 44 (2018) 5273–5283.
  - [50] T. Jia, F. Fu, D. Yu, J. Cao, G. Sun, Facile synthesis and characterization of N-doped TiO<sub>2</sub>/C nanocomposites with enhanced visible-light photocatalytic performance, *Appl. Surf. Sci.* 430 (2018) 438–447.
  - [51] B.R. Strohmaier, An ESCA method for determining the oxide thickness on aluminum alloys, *Surf. Interface Anal.* 15 (1990) 51–56.
  - [52] P.K. Nayak, J. Caraveo-Frescas, Z. Wang, M.N. Hedhili, Q. Wang, H.N. Alshareef, Thin film complementary metal oxide semiconductor (CMOS) device using a single-step deposition of the channel layer, *Sci. Rep.* 4 (2014) 4672.
  - [53] T. Song, Q. Liu, J. Liu, W. Yang, R. Chen, X. Jing, K. Takahashi, J. Wang, Fabrication of super slippery sheet-layered and porous anodic aluminium oxide surfaces and its anticorrosion property, *Appl. Surf. Sci.* 355 (2015) 495–501.
  - [54] W. Zhang, P. Li, H. Xu, R. Sun, P. Qing, Y. Zhang, Thermal decomposition of ammonium perchlorate in the presence of Al(OH)<sub>3</sub>·Cr(OH)<sub>3</sub> nanoparticles, *J. Hazard. Mater.* 268 (2014) 273–280.

- [55] E. Ioannidou, A. Ioannidi, Z. Frontistis, M. Antonopoulou, C. Tselios, D. Tsikritzis, I. Konstantinou, S. Kennou, D.I. Kondarides, D. Mantzavinos, Correlating the properties of hydrogenated titania to reaction kinetics and mechanism for the photocatalytic degradation of bisphenol A under solar irradiation, *Appl. Catal., B* 188 (2016) 65–76.
- [56] H. Liu, T. Lv, C. Zhu, X. Su, Z. Zhu, Efficient synthesis of MoS<sub>2</sub> nanoparticles modified TiO<sub>2</sub> nanobelts with enhanced visible-light-driven photocatalytic activity, *J. Mol. Catal. A: Chem.* 396 (2015) 136–142.
- [57] L. Zeng, Z. Lu, M. Li, J. Yang, W. Song, D. Zeng, C. Xie, A modular calcination method to prepare modified N-doped TiO<sub>2</sub> nanoparticle with high photocatalytic activity, *Appl. Catal., B* 183 (2016) 308–316.
- [58] Q. Sun, K. Lv, Z. Zhang, M. Li, B. Li, Effect of contact interface between TiO<sub>2</sub> and g-C<sub>3</sub>N<sub>4</sub> on the photoreactivity of g-C<sub>3</sub>N<sub>4</sub>/TiO<sub>2</sub> photocatalyst: (0 0 1) vs (1 0 1) facets of TiO<sub>2</sub>, *Appl. Catal., B* 164 (2015) 420–427.
- [59] X. Li, P. Liu, Y. Mao, M. Xing, J. Zhang, Preparation of homogeneous nitrogen-doped mesoporous TiO<sub>2</sub> spheres with enhanced visible-light photocatalysis, *Appl. Catal., B* 164 (2015) 352–359.
- [60] P.G. Smirniotis, T. Boningari, D. Damma, S.N.R. Inturi, Single-step rapid aerosol synthesis of N-doped TiO<sub>2</sub> for enhanced visible light photocatalytic activity, *Catal. Commun.* 113 (2018) 1–5.
- [61] Y. Bai, L. Ye, L. Wang, X. Shi, P. Wang, W. Bai, P.K. Wong, g-C<sub>3</sub>N<sub>4</sub>/Bi<sub>4</sub>O<sub>5</sub>I<sub>2</sub> heterojunction with I<sub>3</sub><sup>-</sup>/I<sup>-</sup> redox mediator for enhanced photocatalytic CO<sub>2</sub> conversion, *Appl. Catal., B* 194 (2016) 98–104.
- [62] K.A. Borges, L.M. Santos, R.M. Paniago, N.M.B. Neto, J. Schneider, D.W. Bahnemann, A.O.T. Patrocínio, A.E.H. Machado, Characterization of a highly efficient N-doped TiO<sub>2</sub> photocatalyst prepared via factorial design, *New J. Chem.* 40 (2016) 7846–7855.
- [63] J. Pan, Z. Dong, B. Wang, Z. Jiang, C. Zhao, J. Wang, C. Song, Y. Zheng, C. Li, The enhancement of photocatalytic hydrogen production via Ti<sup>3+</sup> self-doping black TiO<sub>2</sub>/g-C<sub>3</sub>N<sub>4</sub> hollow core-shell nano-heterojunction, *Appl. Catal., B* 242 (2019) 92–99.
- [64] Y.C. Zhang, M. Yang, G. Zhang, D.D. Dionysiou, HNO<sub>3</sub>-involved one-step low temperature solvothermal synthesis of N-doped TiO<sub>2</sub> nanocrystals for efficient photocatalytic reduction of Cr (VI) in water, *Appl. Catal., B* 142 (2013) 249–258.
- [65] G. Yang, Z. Jiang, H. Shi, T. Xiao, Z. Yan, Preparation of highly visible-light active N-doped TiO<sub>2</sub> photocatalyst, *J. Mater. Chem.* 20 (2010) 5301–5309.
- [66] F.-T. Li, Y. Zhao, Y.-J. Hao, X.-J. Wang, R.-H. Liu, D.-S. Zhao, D.-M. Chen, N-doped P<sub>25</sub> TiO<sub>2</sub>-amorphous Al<sub>2</sub>O<sub>3</sub> composites: One-step solution combustion preparation and enhanced visible-light photocatalytic activity, *J. Hazard. Mater.* 239 (2012) 118–127.
- [67] A.S. Poursani, A. Nilchi, A. Hassani, M. Shariat, J. Nouri, A novel method for synthesis of nano-γ-Al<sub>2</sub>O<sub>3</sub>: study of adsorption behavior of chromium, nickel, cadmium and lead ions, *Int. J. Environ. Sci. Technol.* 12 (2015) 2003–2014.
- [68] L.A. Stanciu, J.R. Groza, A. Jitianu, M. Zaharescu, Structural evolution during reaction to form aluminum titanate from sol-gel precursors, *Mater. Manuf. Processes* 19 (2004) 641–650.
- [69] D. Sarkar, C.K. Ghosh, S. Mukherjee, K.K. Chattopadhyay, Three dimensional Ag<sub>2</sub>O/TiO<sub>2</sub> type-II (p-n) nanoheterojunctions for superior photocatalytic activity, *ACS Appl. Mater. Interfaces* 5 (2012) 331–337.
- [70] Y. Yang, F. Teng, Y. Kan, L. Yang, Z. Liu, W. Gu, A. Zhang, W. Hao, Y. Teng, Investigation of the charges separation and transfer behavior of BiOCl/BiF<sub>3</sub> heterojunction, *Appl. Catal., B* 205 (2017) 412–420.
- [71] K. Li, S. Gao, Q. Wang, H. Xu, Z. Wang, B. Huang, Y. Dai, J. Lu, In-situ-reduced synthesis of Ti<sup>3+</sup> self-doped TiO<sub>2</sub>/g-C<sub>3</sub>N<sub>4</sub> heterojunctions with high photocatalytic performance under LED light irradiation, *ACS Appl. Mater. Interfaces* 7 (2015) 9023–9030.
- [72] L. Xu, X. Ma, N. Sun, F. Chen, Bulk oxygen vacancies enriched TiO<sub>2</sub> and its enhanced visible photocatalytic performance, *Appl. Surf. Sci.* 441 (2018) 150–155.
- [73] W. Wang, M.O. Tadé, Z. Shao, Nitrogen-doped simple and complex oxides for photocatalysis: a review, *Prog. Mater. Sci.* 92 (2018) 33–63.
- [74] J. Meng, Q. Lin, T. Chen, X. Wei, J. Li, Z. Zhang, Oxygen vacancy regulation on tungsten oxides with specific exposed facets for enhanced visible-light-driven photocatalytic oxidation, *Nanoscale* 10 (2018) 2908–2915.
- [75] Z. Zhang, J.T. Yates Jr, Direct observation of surface-mediated electron–hole pair recombination in TiO<sub>2</sub> (110), *The J. Phys. Chem. C* 114 (2010) 3098–3101.
- [76] K. Selvam, M. Swaminathan, Nano N-TiO<sub>2</sub> mediated selective photocatalytic synthesis of quinaldines from nitrobenzenes, *RSC Adv.* 2 (2012) 2848–2855.
- [77] A. Murphy, Band-gap determination from diffuse reflectance measurements of semiconductor films, and application to photoelectrochemical water-splitting, *Sol. Energy Mater. Sol. Cells* 91 (2007) 1326–1337.
- [78] H. Liu, A. Raza, A. Aili, J. Lu, A. AlGhaferi, T. Zhang, Sunlight-sensitive anti-fouling nanostructured TiO<sub>2</sub> coated Cu meshes for ultrafast oily water treatment, *Sci. Rep.* 6 (2016) 25414.
- [79] T. Su, Y. Yang, Y. Na, R. Fan, L. Li, L. Wei, B. Yang, W. Cao, An insight into the role of oxygen vacancy in hydrogenated TiO<sub>2</sub> nanocrystals in the performance of dye-sensitized solar cells, *ACS Appl. Mater. Interfaces* 7 (2015) 3754–3763.
- [80] S. Gahlawat, J. Singh, A.K. Yadav, P.P. Ingole, Exploring Burstein-Moss type effects in nickel doped hematite dendrite nanostructures for enhanced photoelectrochemical water splitting, *Phys. Chem. Chem. Phys.* 21 (2019) 20463–20477.
- [81] A. Riaz, A. Ashraf, H. Taimoor, S. Javed, M.A. Akram, M. Islam, M. Mujahid, I. Ahmad, K. Saeed, Photocatalytic and Photostability Behavior of Ag-and/or Al-Doped ZnO Films in Methylene Blue and Rhodamine B under UV-C Irradiation, *Coat.* 9 (2019) 202.
- [82] D. Yang, M.A. Gondal, Z.H. Yamani, U. Baig, X. Qiao, G. Liu, Q. Xu, D. Xiang, J. Mao, K. Shen, 532 nm nanosecond pulse laser triggered synthesis of ZnO<sub>2</sub> nanoparticles via a fast ablation technique in liquid and their photocatalytic performance, *Mater. Sci. Semicond. Process.* 57 (2017) 124–131.
- [83] X. Meng, Z. Li, J. Chen, H. Xie, Z. Zhang, Enhanced visible light-induced photocatalytic activity of surface-modified BiOBr with Pd nanoparticles, *Appl. Surf. Sci.* 433 (2018) 76–87.
- [84] R.-B. Wei, Z.-L. Huang, G.-H. Gu, Z. Wang, L. Zeng, Y. Chen, Z.-Q. Liu, Dual-cocatalysts decorated rimous CdS spheres advancing highly-efficient visible-light photocatalytic hydrogen production, *Appl. Catal., B* 231 (2018) 101–107.
- [85] Y. Wang, J. Zhao, Z. Chen, F. Zhang, W. Guo, H. Lin, F. Qu, Construction of Z-scheme MoSe<sub>2</sub>/CdSe Hollow Nanostructure with Enhanced Full Spectrum Photocatalytic Activity, *Appl. Catal., B* (2018).
- [86] Y. Guo, J. Tang, Z. Wang, Y.-M. Kang, Y. Bando, Y. Yamauchi, Elaborately assembled core-shell structured metal sulfides as a bifunctional catalyst for highly efficient electrochemical overall water splitting, *Nano Energy* 47 (2018) 494–502.
- [87] X. Ye, Y. Chen, Y. Wu, X. Zhang, X. Wang, S. Chen, Constructing a system for effective utilization of photogenerated electrons and holes: Photocatalytic selective transformation of aromatic alcohols to aromatic aldehydes and hydrogen evolution over Zn<sub>3</sub>In<sub>2</sub>S<sub>6</sub> photocatalysts, *Appl. Catal., B* 242 (2019) 302–311.
- [88] S.J. Hong, S. Lee, J.S. Jang, J.S. Lee, Heterojunction BiVO<sub>4</sub>/WO<sub>3</sub> electrodes for enhanced photoactivity of water oxidation, *Energy Environ. Sci.* 4 (2011) 1781–1787.
- [89] W. Luo, Z. Li, X. Jiang, T. Yu, L. Liu, X. Chen, J. Ye, Z. Zou, Correlation between the band positions of (SrTiO<sub>3</sub>)<sub>1-x</sub>(LaTiO<sub>3</sub>)<sub>2</sub> solid solutions and photocatalytic properties under visible light irradiation, *Phys. Chem. Chem. Phys.* 10 (2008) 6717–6723.
- [90] H. Wang, D. Wu, C. Liu, J. Guan, J. Li, P. Huo, X. Liu, Q. Wang, Y. Yan, Fabrication of Ag/In<sub>2</sub>O<sub>3</sub>/TiO<sub>2</sub>/HNTs hybrid-structured and plasma effect photocatalysts for enhanced charges transfer and photocatalytic activity, *J. Ind. Eng. Chem.* 67 (2018) 164–174.
- [91] M. Yagi, S. Maruyama, K. Sone, K. Nagai, T. Norimatsu, Preparation and photoelectrocatalytic activity of a nano-structured WO<sub>3</sub> platelet film, *J. Solid State Chem.* 181 (2008) 175–182.
- [92] Z. Wang, C. Yang, T. Lin, H. Yin, P. Chen, D. Wan, F. Xu, F. Huang, J. Lin, X. Xie, Visible-light photocatalytic, solar thermal and photoelectrochemical properties of aluminium-reduced black titania, *Energy Environ. Sci.* 6 (2013) 3007–3014.